MIT Libraries | DSpace@MIT

MIT Open Access Articles

Molecular mechanics and structure of the fluid-solid interface in simple fluids

The MIT Faculty has made this article openly available. ***Please share*** how this access benefits you. Your story matters.

Citation: Wang, Gerald J. and Nicolas G. Hadjiconstantinou. "Molecular mechanics and structure of the fluid-solid interface in simple fluids." Physical Review Fluids 2, 9 (September 2017): 094201 © 2017 American Physical Society

As Published: http://dx.doi.org/10.1103/PhysRevFluids.2.094201

Publisher: American Physical Society

Persistent URL: http://hdl.handle.net/1721.1/114562

Version: Final published version: final published article, as it appeared in a journal, conference proceedings, or other formally published context

Terms of Use: Article is made available in accordance with the publisher's policy and may be subject to US copyright law. Please refer to the publisher's site for terms of use.

Massachusetts Institute of Technology

PHYSICAL REVIEW FLUIDS **2**, 094201 (2017)

Molecular mechanics and structure of the fluid-solid interface in simple fluids

Gerald J. Wang and Nicolas G. Hadjiconstantinou[*]
Department of Mechanical Engineering, Massachusetts Institute of Technology,
Cambridge, Massachusetts 02139, USA

(Received 7 May 2017; published 5 September 2017)

Near a fluid-solid interface, the fluid spatial density profile is highly nonuniform at the molecular scale. This nonuniformity can have profound effects on the dynamical behavior of the fluid and has been shown to play an especially important role when modeling a wide variety of nanoscale heat and momentum transfer phenomena. We use molecular-mechanics arguments and molecular-dynamics (MD) simulations to develop a better understanding of the structure of the first fluid layer directly adjacent to the solid in the layering regime, as delineated by a nondimensional number that compares the effects of wall-fluid interaction to thermal energy. Using asymptotic analysis of the Nernst-Planck equation, we show that features of the fluid density profile close to the wall, such as the areal density of the first layer Σ_{FL} (defined as the number of atoms in this layer per unit of fluid-solid interfacial area), can be expressed as polynomial functions of the fluid average density ρ_{ave}. This is found to be in agreement with MD simulations, which also show that the width of the first layer h_{FL} is a linear function of the average density and only a weak function of the temperature T. These results can be combined to show that, for system average densities corresponding to a dense fluid ($\rho_{\mathrm{ave}} \geqslant 0.7$), the ratio $\mathcal{C} \equiv \frac{\Sigma_{\mathrm{FL}}}{\rho_{\mathrm{ave}} h_{\mathrm{FL}}}$, representing a density enhancement with respect to the bulk fluid, depends only weakly on temperature and is essentially independent of density. Further MD simulations suggest that the above results, nominally valid for large systems (solid in contact with semi-infinite fluid), also describe fluid-solid interfaces under considerable nanoconfinement, provided ρ_{ave} is appropriately defined.

DOI: 10.1103/PhysRevFluids.2.094201

I. INTRODUCTION

Nanoconfined fluids exhibit many remarkable properties [1–3], with considerable potential engineering applications in fields as far ranging as nanoscale filtration and desalination [4–6], carbon sequestration in nanoporous media [7], nanoscale energy harvesting [8], enhanced chemical sensing [9], and nanoscale drug delivery [10]. As rapid advances continue to be made in the field of nanofluidic devices, developing physical models of nanoscale effects near the liquid-solid interface becomes increasingly important, since these effects can significantly affect the liquid's structure as well as hydrodynamic behavior.

In particular, it is well known that a fluid in the vicinity of a solid boundary will adopt a layered structure in response to interactions with solid atoms [11–13]. These layers have a profound effect on key fluid properties. Early work focused on the phenomenology of layer formation, including the structural features of adsorbed layers [14] and their implications for tribological applications [15]. More recently, several groups have reported that when a nanoconfining structure (e.g., a carbon nanotube or a graphene nanoslit) is held in equilibrium with a large reservoir of fluid, the density of the fluid confined within the nanostructure is measured to be substantially less than the density of the fluid reservoir [16–18]. This density anomaly has been shown to be the direct result of fluid layering [19]. Layering has also been shown to be closely related to the solvation pressure in nanoconfined fluids [20,21].

Beyond its relation to static properties, fluid layering also has significant effects on several nanoscale transport phenomena of practical interest. Notably, it has been proposed that fluid

---

[*] Corresponding author: ngh@mit.edu

©2017 American Physical Society

structuring in the vicinity of the fluid-solid interface plays an important role in determining the slip length in the fluid; in particular, it has been shown that, under some conditions, the slip length is inversely proportional to the density of the first fluid layer at the interface [22]; the relationship between the interfacial contact density and slip length has also been investigated experimentally [23]. Similarly, molecular-dynamics (MD) simulations [24], as well as experiments [25], have shown that the thermal resistance at the liquid-solid interface depends strongly on the magnitude of fluid layering at the interface (in fact, this connection between interfacial fluid structure and thermal resistance was recently extended to liquid-vapor systems [26]). Since the first fluid layer can be of considerably higher density than the bulk, it is possible that this layer may be able to support phononlike modes, which has profound implications for solid-to-liquid heat transfer in nanoscale devices [27]. As a consequence, it may be possible to indirectly control the slip length and thermal resistance in a nanofluidic device by directly controlling the magnitude of structuring at the interface. This could be accomplished, for example, by tuning the fluid-solid interaction strength [27–29] or strain engineering [30].

From the perspective of efficient and accurate multiscale simulation, it is highly desirable to incorporate molecular-scale features into macroscopic (continuum) solvers [31]. If information about the spatially varying density profile near the solid-liquid interface is known, then this information could be used to improve the modeling capabilities of efficient continuum solvers for nanofluidic systems.

The critical role of the interfacial fluid structure, in nanoscale science, engineering, and simulation methods development, strongly motivates the need for models that can describe and predict its characteristic length scales and density variations. Although the interfacial fluid structure typically exhibits several pronounced fluid layers (depending on factors such as the fluid-solid interaction strength or the temperature), this layering effect decays as one moves away from the interface. As a result, in this study we will focus on the layer closest to the interface, which is the most distinctly defined and most influential for anomalous interfacial phenomena; we will refer to this layer as the first layer. We also note that the interfacial fluid structure can be accurately described using liquid-state density-functional theory [32]; in contrast, our focus here is on developing a less complex model that highlights the basic molecular-mechanical factors governing the structure of the first fluid layer. Finally, we note that our work exploits the observation that, for typical problems of interest, transport (nonequilibrium) introduces negligible change [33] to the equilibrium fluid structure at the fluid-wall interface; in other words, although in this paper we study equilibrium systems, we expect our results to be directly applicable to the nonequilibrium situations of interest discussed above.

The paper is organized as follows. In Sec. II we study the structure of the first fluid layer in semi-infinite systems using MD simulations and molecular mechanics arguments. We introduce a nondimensional number that identifies the conditions under which significant layering is observed and develop molecular models for the width and number density associated with the first fluid layer. In Sec. III we show that our results for infinite systems also hold for finite systems as well as systems under nanoconfinement, provided the average fluid density is appropriately defined. We finish with a summary and discussion of our results in Sec. IV.

II. MODELING AND SIMULATION IN SEMI-INFINITE SYSTEMS

We consider a fluid whose atoms interact via the Lennard-Jones (LJ) [34] potential

$$u^*_{ff}(r) = 4\varepsilon^*_f\left[\left(\frac{\sigma^*_f}{r^*}\right)^{12} - \left(\frac{\sigma^*_f}{r^*}\right)^{6}\right]. \tag{1}$$

The fluid rests in a slitlike geometry, bounded in the z direction by two solid boundaries (walls). The distance between the two boundaries is denoted by L^*. The interaction between the fluid and the boundaries is also of the LJ type with parameters ε^* and σ^* and is denoted by u^*_{wf}. Throughout this work, asterisks denote dimensional quantities; unless otherwise stated, nondimensional quantities are scaled by the LJ length scale σ^*, energy scale ε^*, and temperature scale ε^*/k_B, where k_B is Boltzmann's constant.

For the majority of the MD results presented in this work, the solid boundaries are composed of one graphene sheet held rigid with periodic boundary conditions in all directions; the effect of multiple rigid graphene layers as well as nonrigid walls is discussed in the Appendix. More details on the MD simulations can also be found in the Appendix.

We begin the investigation by considering the semi-infinite fluid case, where L is sufficiently large that a well-defined bulk-fluid region separates the fluid-solid interfaces such that they have negligible effect on each other (in practice, $L \geqslant 30$ suffices; in our simulations, $L = 32$). Finite systems are discussed in Sec. III. Our simulations are performed within the temperature range $0.6 \leqslant T \leqslant 20$ and within the average density range $0.4 \leqslant \rho_{\text{ave}} \leqslant 1.2$. Here $\rho_{\text{ave}} \equiv \frac{N_{\text{tot}}\sigma^{*3}}{V^*_{\text{acc}}}$, where V^*_{acc} is the volume accessible to the fluid; this quantity is more precisely defined in the next section. The models that we present are valid within the layering regime, i.e., conditions under which distinct fluid layers form, which we will now discuss.

A. Wall number and layering regime

The concepts of layering that we develop in the following sections presume the presence of at least one distinct layer (i.e., a pronounced first peak in the fluid spatial density profile). Generally speaking, layering occurs when the wall-fluid interaction is relatively strong; in particular, layering occurs when the energy scale of fluid-wall interaction in the interfacial region is large compared the energy scale of thermal motion (which generally tends to discourage the formation of ordered structures). Given the above, and approximating the wall as an infinite plane with a density of n^* atoms per unit area, we define the Wall number $\text{Wa} \equiv \frac{n^*\sigma^{*2}\varepsilon^*}{k_B T^*}$ as a measure of the relative importance of wall-fluid interaction energy (proportional to $n^*\sigma^{*2}\varepsilon^*$) to thermal energy (proportional to $k_B T^*$). From its definition we expect that $\text{Wa} \ll 1$ will indicate relatively small inhomogeneity in the spatial density profile near the wall, whereas $\text{Wa} \not\ll 1$ will correspond to the presence of well-defined layering. As stated above, this work focuses on the strongly layering regime denoted by $\text{Wa} \not\ll 1$. Given the nondimensional set of units used throughout this paper, we note that, in these units, $\text{Wa} = \frac{n}{T}$, where $n = n^*\sigma^{*2}$.

To quantify the notion of a well-defined first layer, we also define the degree of layering as $\mathcal{L} = \frac{\max_z \rho(z)}{\min_{\sigma \leqslant z \leqslant 2\sigma} \rho(z)}$, where $\rho(z)$ is the fluid spatial density profile in the direction orthogonal to the fluid-solid interface. From MD simulations, we find that $\mathcal{L} \gtrsim 5$ is sufficient for the purposes of our modeling below. In Fig. 1 we can clearly see that the degree of layering increases with increasing Wall number; in particular, the layering regime $\mathcal{L} \gtrsim 5$ corresponds to $\text{Wa} \not\ll 1$.

B. Anatomy of the first layer: Length scales of layering and density enhancement

Figure 2 shows the distinct layering of fluid near the liquid-solid interface at $\text{Wa} \not\ll 1$. Characteristic liquid density profiles in the wall vicinity are shown in Fig. 3. From this figure we can see that, in the strongly layering regime, density variations extend up to $\ell_c \sim 5$ from the solid and more than five distinct layers are discernible before the density relaxes to the bulk value ρ_{bulk}. Of particular interest here are the standoff distance between the wall and the fluid, denoted by $z_{\min}$, and the thickness (width) of the first layer, denoted h_{FL}; both are shown in Fig. 3. An additional quantity of interest is the overall particle content of the first layer. These quantities are defined more precisely and discussed in more detail in the sections that follow.

1. *Standoff distance of the first layer*

The standoff between the fluid and the wall is primarily a result of the repulsive interaction between the two substances. As explained in detail in Sec. II C 1, closed-form descriptions of $z_{\min}$ can be obtained by considering the competition between the wall-fluid interaction and thermal energy, using a mean-field theory approach [19]. For the system studied here, this theory predicts

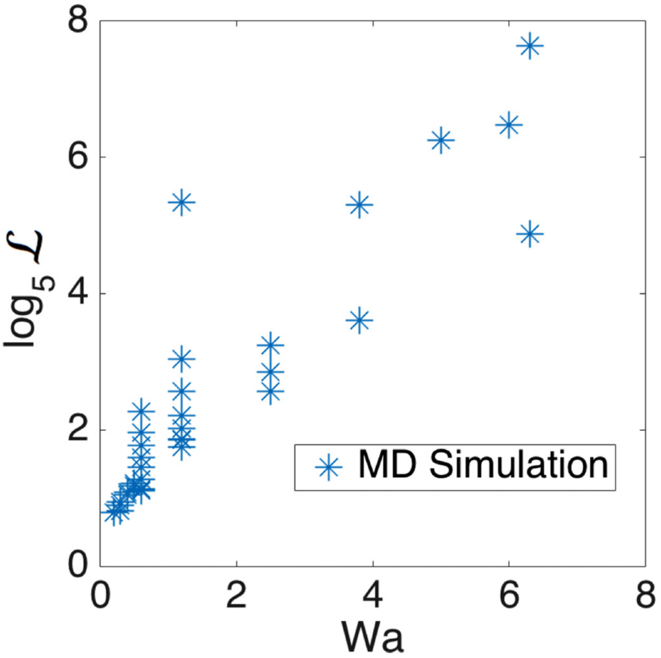

FIG. 1. Relation between degree of layering and Wall number, obtained from 33 MD simulations of a LJ fluid confined within a graphene nanoslit with $0.4 \leqslant \rho_{\text{ave}} \leqslant 1.2$ and $0.6 \leqslant T \leqslant 20$.

$z_{\min} = 0.86$ (Fig. 4), independent of density or temperature. Our MD results, shown in Fig. 4, verify that the mean-field theory prediction is valid for a wide range of temperatures and fluid densities.

As will be seen below, this result has a number of implications. Here we discuss its application to the accessible volume defined above; in a graphene nanoslit geometry, this quantity is given by $V_{\text{acc}} = (L - 2z_{\min})A$, where A is the interfacial contact area between the fluid and the solid. Accounting for the excluded volume due to $z_{\min}$ becomes particularly important in finite systems, where this volume is appreciable compared to the total system volume, as further discussed in Sec. III.

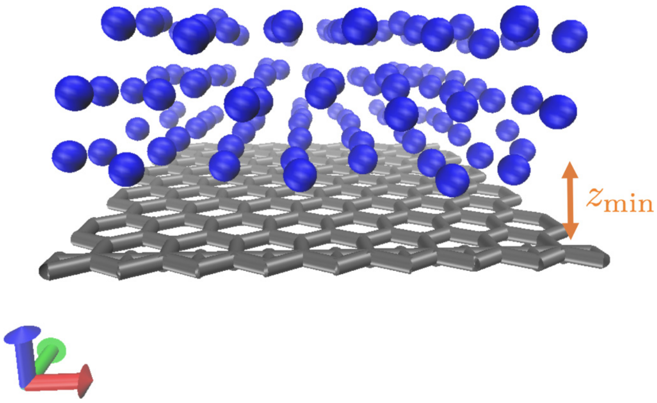

FIG. 2. Fluid layering near the graphene surface, obtained from MD simulation at $T = 6.4$ and $\rho_{\text{ave}} = 1.2$ (Wa = 0.6). The minimum separation $z_{\min}$ is schematically illustrated in orange. Visualization performed using [35].

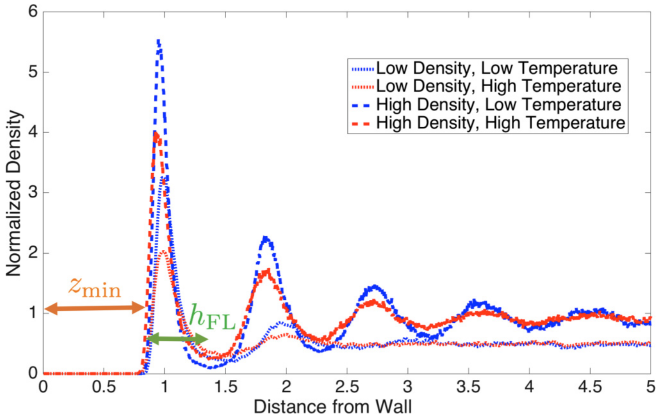

FIG. 3. Four smoothed fluid spatial density profiles, corresponding to a lower density ($\rho_{\mathrm{ave}} = 0.5$) and a higher density ($\rho_{\mathrm{ave}} = 1.0$) as well as a lower temperature ($T = 3.2$) and a higher temperature ($T = 6.4$). In all cases, density variations are low in amplitude at a distance of 5σ from the wall. The first-layer width h_{FL} is schematically illustrated in green. Note that h_{FL} is a function of density and also a weak function of temperature in the low-density case. The minimum separation z_{min} given in Eq. (3) is schematically illustrated in orange. Note that this quantity does not discernibly depend on density or temperature.

2. *First-layer width*

We define the first-layer width, denoted by h_{FL}, as the distance between z_{min} and the first nonzero minimum of the density profile. This distance is shown schematically in Fig. 3. To prevent small density fluctuations over space from materially affecting the calculation of the first nonzero

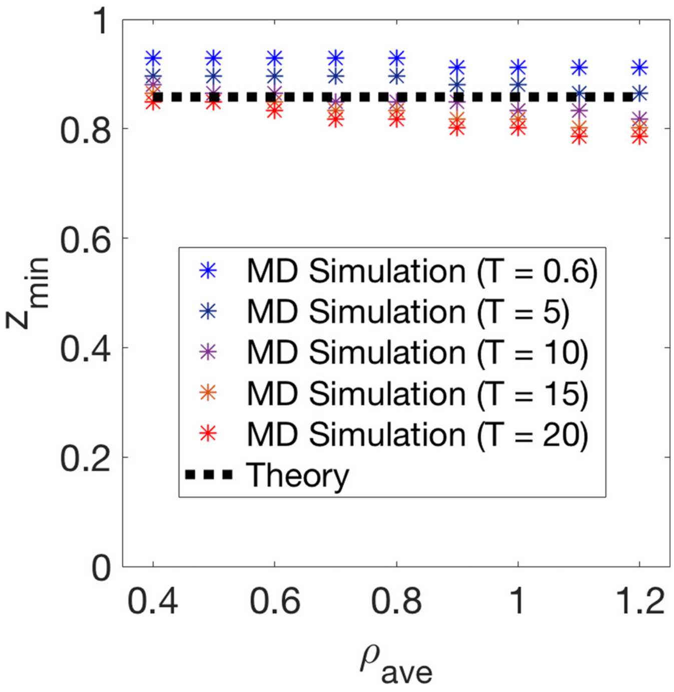

FIG. 4. Molecular-dynamics results ($0.6 \leqslant T \leqslant 20$) for the standoff distance z_{min} are shown as a function of density, along with the value predicted by mean-field theory in Eq. (3).

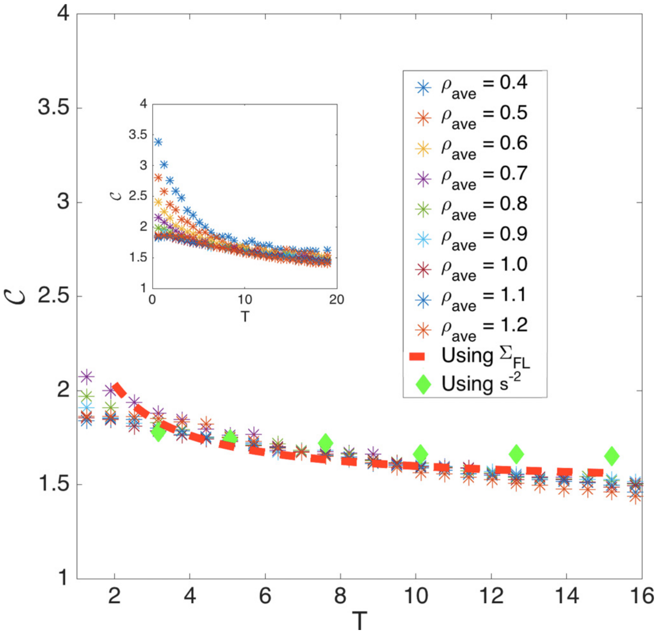

FIG. 5. Density enhancement as a function of temperature for $0.7 \leqslant \rho_{\text{ave}} \leqslant 1.2$ (the inset shows the density enhancement for three additional low densities $0.4 \leqslant \rho_{\text{ave}} \leqslant 0.6$). Note that the density enhancement decreases with increasing temperature for all densities. Moreover, for $\rho_{\text{ave}} \geqslant 0.7$, the enhancement can be accurately modeled using Σ_{FL} from Eq. (18) (represented by the dashed curve) as well as using s^{-2} from Eq. (25) (represented by diamonds).

minimum, we perform moving-average smoothing on the density profile with a window size of 0.5; we have verified that the location of the first nonzero minimum is not affected by the choice of the window size ranging from 0.3 to 1.1. We note that unlike $z_{\min}$, h_{FL} may depend on the temperature and density.

3. *Density enhancement*

Having established the length scales relevant to the first layer, we now define the first-layer density enhancement, a measure of the particle content of the first layer, as $\mathcal{C} \equiv \frac{\rho_{\text{FL}}}{\rho_{\text{ave}}}$. Here ρ_{FL} is the (volumetric) density of fluid molecules contained within $z_{\min} \leqslant z \leqslant z_{\min} + h_{\text{FL}}$. Although it is reasonable to expect that, in general, $\mathcal{C} = \mathcal{C}(\rho, T)$ – for example, the magnitude of the density peaks appear to be quite sensitive to the system density and temperature (see, e.g., Fig. 3) – we also expect that $\lim_{T\to\infty} \mathcal{C}(\rho, T) = 1$, since, in the limit of high temperatures, the fluid spatial density profile should approach a flat distribution across the channel, corresponding to free-energy minimization via entropy maximization.

Surprisingly, Fig. 5 shows that for $\rho_{\text{ave}} \geqslant 0.7$, $\mathcal{C}$ is essentially independent of density not only for $T \to \infty$, but for all $T \gtrsim 6$. Moreover, its temperature dependence is very weak. This remarkable relationship implies that the fluid density in the first layer, based on the width h_{FL}, is related to the average fluid density via a density-independent enhancement factor that is only weakly dependent on temperature.

C. Molecular mechanics of the first layer

In this section we use MD simulations and molecular mechanics modeling to explain the behaviors observed in Sec. II B. In addition to the standoff distance $z_{\min}$ and enhancement factor $\mathcal{C}$, we also define and investigate the behavior of the fluid areal density in the first layer Σ_{FL}.

1. *Standoff distance between the wall and the first layer*

The first fluid layer forms at a characteristic distance from the wall that can be calculated using the mean-field approach proposed in Ref. [19]. Assuming that the solid surfaces are sufficiently large such that edge effects are negligible, the mean-field interaction potential between the solid and a fluid atom at distance z^* from the solid layer is given by

$$U^*_{\text{plane}}(z^*) = \frac{2n\varepsilon^*\pi}{5}\left[2\left(\frac{\sigma^*}{z^*}\right)^{10} - 5\left(\frac{\sigma^*}{z^*}\right)^{4}\right]. \tag{2}$$

As before, n denotes the (nondimensional) areal density of solid atoms in the graphene sheet. This mean-field potential rises sharply as $z^* \to 0$, making regions close to the solid described by $z^* < z^*_{\text{min}}$ inaccessible to the fluid. The value of z^*_{min} can be accurately estimated by setting $U^*_{\text{plane}}(z^*) = 0$. The rationale for this choice is that the rise of $U^*_w(z^*)$ is so sharp that solving for $U^*_{\text{plane}}(z^*) = A^*$, where A^* is some constant ($A^* \sim k_B T^*$), leads to a more cumbersome but for all practical purposes equivalent result. Proceeding, we find

$$z_{\text{min}} = \left(\tfrac{2}{5}\right)^{1/6}. \tag{3}$$

This result is within 8% of the standoff distance observed in Sec. II B 1 for $0.4 \leqslant \rho_{\text{ave}} \leqslant 1.2$ and $0.6 \leqslant T \leqslant 20$. We also note that (3) is identical to the result obtained in Ref. [19] for the standoff distance in a cylindrical geometry (e.g., carbon nanotubes). This is because the effects of curvature do not appear to leading order considered in Ref. [19].

2. *Areal density of the first layer*

It is worth noting that although the first layer is strictly not a two-dimensional structure (since it has a characteristic width of h_{FL}), this layer tends to be narrow. This observation motivates us to characterize its packing using an areal density defined using the relation

$$\Sigma_{\text{FL}} \equiv \rho_{\text{FL}} h_{\text{FL}} = \mathcal{C}\rho_{\text{ave}} h_{\text{FL}}. \tag{4}$$

In principle, $\Sigma_{\text{FL}} = \int_{z_{\text{min}}}^{z_{\text{min}}+h_{\text{FL}}} \rho\, dz$ can be calculated from the solution of the Nernst-Planck equation [36]

$$\frac{d^2\rho^*}{dz^{*2}} = -\frac{d}{dz^*}\left(\frac{\rho^*}{k_B T^*}\frac{dU^*}{dz^*}\right) \tag{5}$$

describing the particle number density as a function of the distance from the wall. Here $U^*(z^*) = U^*_w(z^*) + U^*_f(z^*,\rho^*(z^*))$ is the potential energy per particle, which decomposes into the potential energy due to the solid-fluid interaction $U^*_w(z^*)$ and the potential energy due to the fluid-fluid interaction $U^*_f(z^*,\rho^*(z^*))$. These two quantities can be calculated from

$$U^*_w(z^*) = n^* \int_{\Omega^*_w} u^*_{wf}[r^*(z^*,x^{*\prime},y^{*\prime},z^{*\prime})]d\Omega^*_w(x^{*\prime},y^{*\prime},z^{*\prime}) \tag{6}$$

and

$$\begin{aligned} U^*_f(z^*) &= \int_{\Omega^*_f} u^*_{ff}[r^*(z^*,x^{*\prime},y^{*\prime},z^{*\prime})]\rho^*(z^{*\prime})d\Omega^*_f(x^{*\prime},y^{*\prime},z^{*\prime}) \\ &= \rho_{\text{ave}}\varepsilon^*_f \int_{\Omega_f} u_{ff}[r(z,x',y',z')]\tilde{\rho}(z')d\Omega_f(x',y',z'), \end{aligned} \tag{7}$$

where Ω_w and Ω_f denote the wall and fluid domains, respectively, and $\tilde{\rho} = \rho/\rho_{\text{ave}}$. We note that Eq. (6) simply evaluates to the result of Eq. (2) for the case of the graphene walls studied in this work. From the above two expressions we see that $U^*_w \sim n\varepsilon^*$, while $U^*_f \sim \rho_{\text{ave}}\varepsilon^*_f$.

Equation (5) can be integrated once to yield

$$\frac{d\rho^*}{dz^*} = -\frac{\rho^*}{k_B T^*}\frac{dU^*}{dz^*}. \tag{8}$$

This equation needs to be solved subject to the constraint

$$\int_0^{L^*} \rho^*(z^*)dz^* = \rho^*_{\text{ave}} L^*. \tag{9}$$

Taking into consideration the dominant role of the solid boundary in the vicinity of the solid-fluid interface, we write

$$\frac{U_w^*(z^*)}{k_B T^*} = \frac{n}{T} U_w(z^*), \tag{10}$$

$$\frac{U_f^*(z^*,\rho^*(z^*))}{k_B T^*} = \frac{\rho_{\text{ave}}\varepsilon_f^*}{\varepsilon^* T} U_f(z^*,\tilde{\rho}(z^*)) = \epsilon \frac{n}{T} U_f(z^*,\tilde{\rho}(z^*)), \tag{11}$$

where $\epsilon = \rho_{\text{ave}}\varepsilon_f^*/n\varepsilon^*$. Equation (8) can thus be written as

$$\frac{d\tilde{\rho}}{dz} = -\text{Wa}\tilde{\rho}\left(\frac{dU_w}{dz} + \epsilon\frac{dU_f(\tilde{\rho})}{dz}\right). \tag{12}$$

Based on the structure of this equation and the observation that typically $\epsilon \ll 1$ (in our simulations $\epsilon \approx 0.2$), we propose a solution of the form

$$\tilde{\rho} = \sum_{j=0}^{\infty} \epsilon^j \tilde{\rho}_j, \tag{13}$$

recalling that $\epsilon \propto \rho_{\text{ave}}$. Using Eq. (13), we find to zeroth order

$$\frac{d\tilde{\rho}_0}{dz} = -\text{Wa}\tilde{\rho}_0\frac{dU_w}{dz}, \tag{14}$$

while at the next order we find

$$\frac{d\tilde{\rho}_1}{dz} = -\text{Wa}\tilde{\rho}_1\frac{dU_w}{dz} - \text{Wa}\tilde{\rho}_0\frac{dU_f(\tilde{\rho}_0)}{dz}. \tag{15}$$

Equation (14) can be solved directly using the constraint $\int_0^L \tilde{\rho}_0 dz = L$. Subsequently, given $\tilde{\rho}_0$, Eq. (15) can be solved subject to the constraint $\int_0^L \tilde{\rho}_1 dz = 0$.

Ultimately, a numerical treatment is required due to the complexity associated with evaluating $U_f(\tilde{\rho}_j)$. Given that "exact" solutions (to all orders of ϵ) of the above problem are available via MD simulation, we leave numerical implementation to future work. Here we use the above solution framework to make some general deductions in support of our MD simulation results. In particular, from the above discussion we can see that

$$\rho(z) = \rho_{\text{ave}}[\rho_0(z) + \epsilon\rho_1(z) + O(\epsilon^2)]. \tag{16}$$

This confirms that in the regime $\{\text{Wa} \not\ll 1, \epsilon \ll 1\}$ features of the fluid local density can be described in polynomial expansions of the average fluid density. In other words, we expect that

$$\Sigma_{\text{FL}}(\rho_{\text{ave}},T) = \sum_{j=1}^{\infty} a_j(T)\rho_{\text{ave}}^j. \tag{17}$$

To validate the above result, we conducted MD simulations over a range of densities and temperatures such that $\text{Wa} \not\ll 1$. As shown in Figs. 5 and 6, we find that our MD results can be

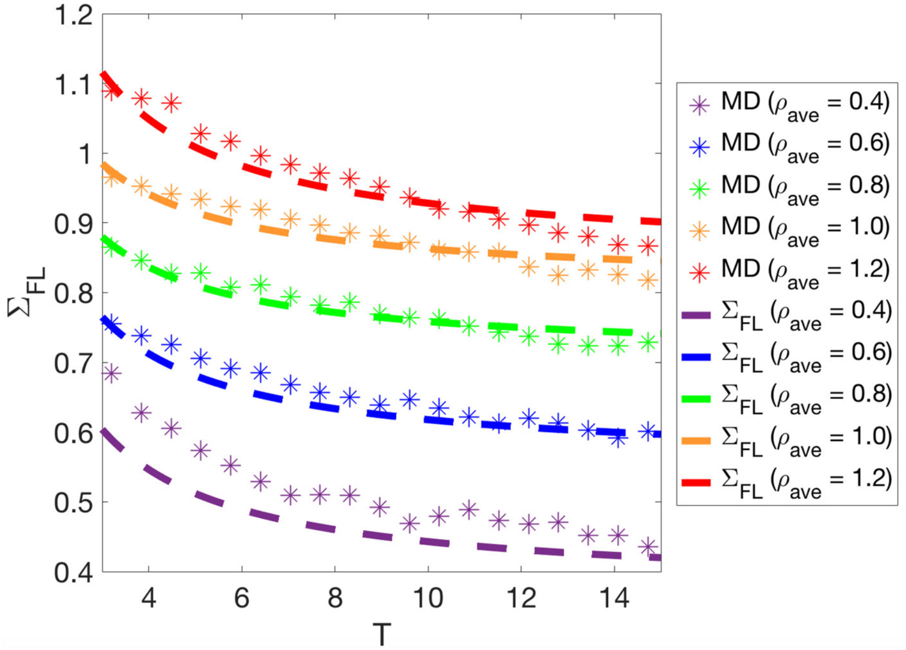

FIG. 6. Molecular-dynamics results for the first-layer areal densities Σ_{FL} as a function of temperature T. Equation (18), represented by dashed curves, is able to capture these values of Σ_{FL} accurately (especially for $\rho_{\mathrm{ave}} \geqslant 0.6$).

described quite accurately in the range $0.4 \leqslant \rho_{\mathrm{ave}} \leqslant 1.2$ and $2 \leqslant T \leqslant 15$ using the form

$$\Sigma_{\mathrm{FL}}(\rho_{\mathrm{ave}}, T) = a_1(T)\rho_{\mathrm{ave}} + a_2(T)\rho_{\mathrm{ave}}^2 + a_3(T)\rho_{\mathrm{ave}}^3, \tag{18}$$

where

$$\begin{aligned} a_1(T) &= 0.994 + 4.797T^{-1} = 0.994 + 1.267\,\mathrm{Wa} = a_1(\mathrm{Wa}),\\ a_2(T) &= 0.071 - 8.738T^{-1} = 0.071 - 2.307\,\mathrm{Wa} = a_2(\mathrm{Wa}),\\ a_3(T) &= -0.258 + 4.431T^{-1} = -0.258 + 1.170\,\mathrm{Wa} = a_3(\mathrm{Wa}). \end{aligned}$$

Here we note that the functional form of coefficients a_1, a_2, a_3 [and consequently $\Sigma_{\mathrm{FL}}(\rho_{\mathrm{ave}}, T) = \Sigma_{\mathrm{FL}}(\rho_{\mathrm{ave}}, \mathrm{Wa})$] can be motivated by the expected form of the solutions to Eqs. (14) and (15).

3. Variation of first-layer width with average density

In view of the definition (4) and Eq. (17) from the preceding section, in this section we examine the dependence of the first-layer width h_{FL} on the fluid density. In Fig. 7 we show MD simulation results for the first-layer width plotted as a function of temperature for a variety of system average densities. We note a clear dependence of h_{FL} on ρ_{ave}, but a weak dependence on temperature. Motivated by this observation, we average the first-layer widths across the full range of temperatures; the results are shown in Fig. 8 along with the least-squares linear fit $h_{\mathrm{FL}}(\rho_{\mathrm{ave}}) = h_0 - k\rho_{\mathrm{ave}}$, where $h_0 = 0.80$ and $k = 0.30$. These results strongly suggest that the first-layer width can be accurately represented as a first-degree polynomial in ρ_{ave}.

In the remainder of this section we use the results of the Nernst-Planck analysis of the preceding section to provide some motivation for this result. We start by noting that h_{FL} can be defined as the distance between the first density minimum and the standoff location identified by z_{min}. We also note that to an excellent approximation z_{min} is independent of the fluid density. These two observations

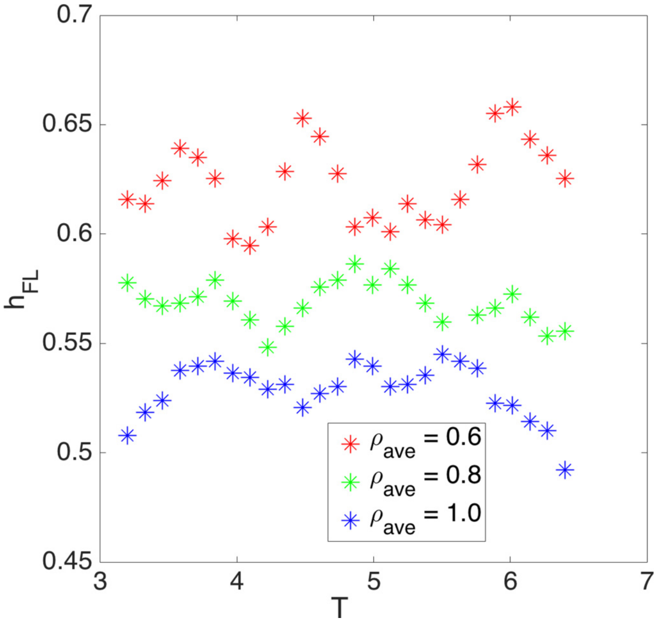

FIG. 7. The first-layer width h_{FL} is shown for three different densities and $3.2 \leqslant T \leqslant 6.4$. Note that h_{FL} is clearly a function of ρ_{ave} but only a weak function of temperature.

mean that the dependence of h_{FL} on the density is the same as the dependence of the first minimum of Eq. (16) on the density. To leading order in ϵ, any extremum of Eq. (16) located at $z = Z$ obeys

$$\frac{d\rho_0}{dz}(z = Z) + \epsilon \frac{d\rho_1}{dz}(z = Z) = 0. \tag{19}$$

To study the (leading-order) dependence of Z on the density, we differentiate with respect to Z to find

$$\frac{d^2\rho_0}{dZ^2} + \epsilon \frac{d^2\rho_1}{dZ^2} + \frac{d\epsilon}{dZ}\frac{d\rho_1}{dZ} = 0. \tag{20}$$

Solving for $dZ/d\epsilon$, we obtain

$$\frac{dZ}{d\epsilon} = -\frac{d\rho_1/dZ}{d^2\rho_0/dZ^2 + \epsilon d^2\rho_1/dZ^2}, \tag{21}$$

which, in the limit of small ϵ, can be written (to leading order) as

$$Z - Z_A = -\left[\frac{d\rho_1/dZ}{d^2\rho_0/dZ^2}\right]_A (\epsilon - \epsilon_A), \tag{22}$$

where $[\,]_A$ denotes evaluation at the reference condition A. The linearization about point A is justified by the observation that h_{FL} changes very slowly with ρ_{ave}. In summary, we find that, to leading order and under some additional assumptions, our finding that the width of the first layer is to a good approximation linear in the system average density is supported by the Nernst-Planck theory.

4. Another look at dense fluids ($\rho_{ave} \gtrsim 0.7$)

When combined with the definition (4), the dependence of h_{FL} and Σ_{FL} on ρ_{ave} provides the necessary ingredients for explaining the observations of Sec. II B 3, namely, that $\mathcal{C}$ is a weak function of density and in particular $\mathcal{C} = \mathcal{C}(T)$ when $\rho_{\mathrm{ave}} \gtrsim 0.7$. In this section we focus on the

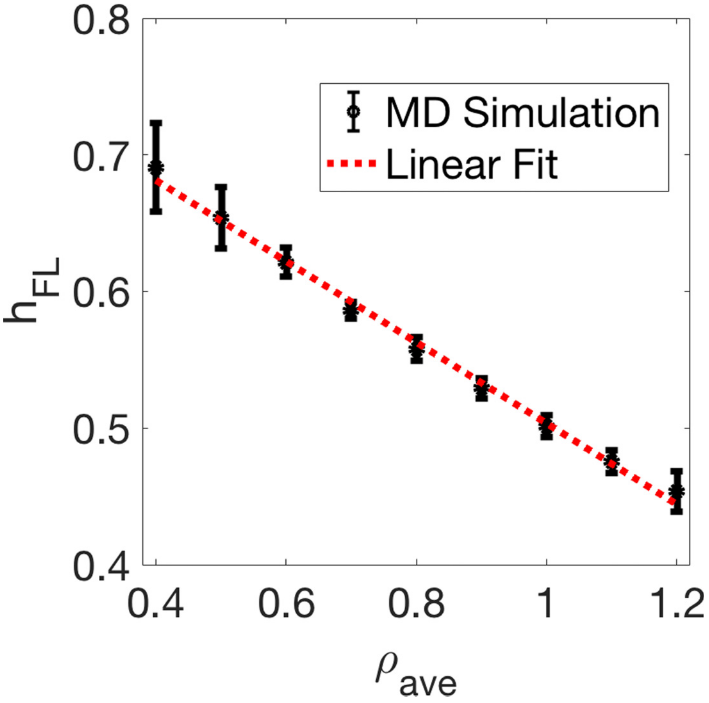

FIG. 8. Molecular-dynamics results for the first-layer width h_{FL} are shown as a function of density, along with a linear fit. The bars indicate the variation of first-layer widths due to temperature in the range $2 \leqslant T \leqslant 20$.

regime $\rho_{\mathrm{ave}} \gtrsim 0.7$ where the result $\mathcal{C} = \mathcal{C}(T)$ requires cancellation between the density dependences of h_{FL} and Σ_{FL}. We also note that, in this regime, it is known that two-dimensional Lennard-Jones materials arrange into hexagonal packing [37]. It is natural to inquire whether the two effects are related.

Assuming a hexagonal structure, the areal density of the first layer can be written in terms of the hexagon side length $s(\rho_{\mathrm{ave}},T)$ as

$$\Sigma_{\mathrm{FL}}(\rho_{\mathrm{ave}},T) = \frac{2}{\sqrt{3}} s(\rho_{\mathrm{ave}},T)^{-2}, \tag{23}$$

where, in accordance with the discussion of Eq. (17), we write

$$s(\rho_{\mathrm{ave}},T)^{-2} = \sum_j b_j(T)\rho_{\mathrm{ave}}^j. \tag{24}$$

To $O(\rho_{\mathrm{ave}}^3)$ the areal density takes the form

$$\Sigma_{\mathrm{FL}}(\rho_{\mathrm{ave}},T) = \frac{2}{\sqrt{3}}\left[b_1(T)\rho_{\mathrm{ave}} + b_2(T)\rho_{\mathrm{ave}}^2 + b_3(T)\rho_{\mathrm{ave}}^3\right]. \tag{25}$$

We determine $b_1(T)$, $b_2(T)$, and $b_3(T)$ from MD simulations of the in-plane structure of the first layer. In particular, we first obtain the radial distribution function in the plane of the layer (the xy plane in Fig. 2) for all fluid atoms within the first layer; this quantity is shown for several densities in Fig. 9. We define $s(\rho_{\mathrm{ave}},T)$ as the distance at which this radial distribution function falls to half of its maximum value. This distance typifies the standoff distance between each atom and its nearest neighbors within the hexagonally packed first layer. We extract values of $s(\rho_{\mathrm{ave}},T)^{-2}$ from MD simulations at a series of temperatures and fit these results to Eq. (25) (Fig. 10).

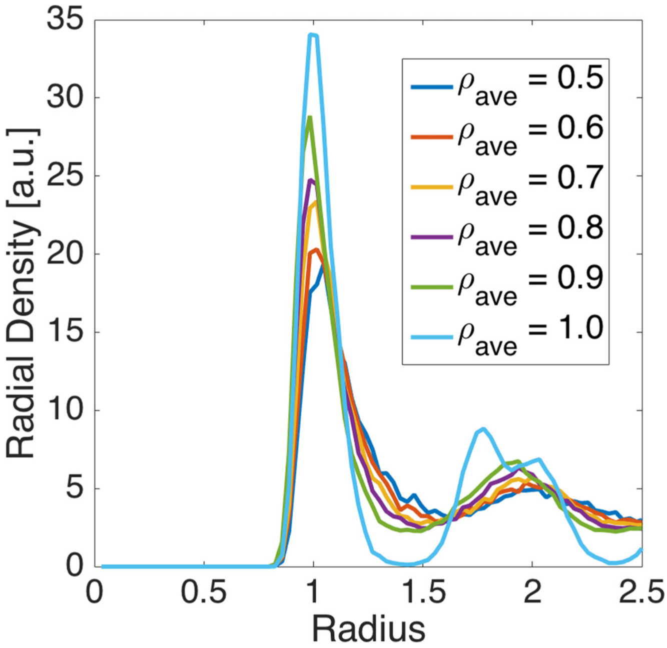

FIG. 9. Radial distribution functions for fluid atoms within the first layer, for systems with six different densities, obtained from MD simulations at $T = 3.8$.

From the empirical fits for $h_{\mathrm{FL}}(\rho_{\mathrm{ave}})$ and $s(\rho_{\mathrm{ave}}, T)$, we find that the density enhancement

$$\mathcal{C} = \frac{2s(\rho_{\mathrm{ave}}, T)^{-2}}{\sqrt{3}\rho_{\mathrm{ave}} h_{\mathrm{FL}}(\rho_{\mathrm{ave}})} \tag{26}$$

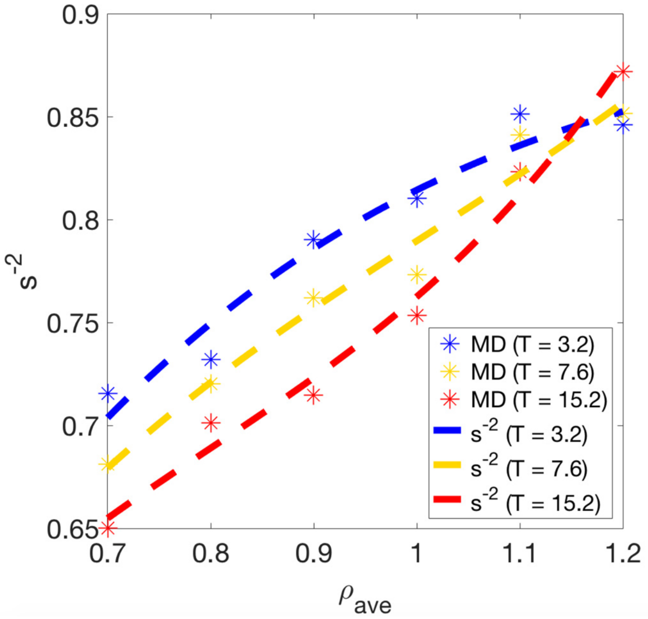

FIG. 10. Molecular-dynamics results and corresponding fits to Eq. (25) for s^{-2}, as a function of ρ_{ave}, at three values of T.

is very slowly varying over the range $0.7 \leqslant \rho_{\text{ave}} \leqslant 1.2$. Thus we can average over ρ_{ave} to obtain a density-independent $\mathcal{C}$ at each temperature. These density-independent values of $\mathcal{C}$ differ, on average, by less than 4% from Eq. (26) for $0.7 \leqslant \rho_{\text{ave}} \leqslant 1.2$ and $2 \leqslant T \leqslant 20$, which is negligible compared to the variation in $\mathcal{C}$ with T over this same range. Values of the density enhancement obtained through this route are shown in Fig. 5 for five temperatures, all of which are within 5% of the values of $\mathcal{C}$ obtained via direct measurement of the first-layer density.

In this section we have seen that the result $\mathcal{C} = \mathcal{C}(T)$ coincides with the arrangement of the first-layer atoms in a two-dimensional structure of hexagonal symmetry. The resulting structure is sufficiently ordered that the areal density of the layer as a function of T and ρ_{ave} can be accurately recovered from measurement of the characteristic spacing between atoms. It is still unclear whether the relation $\rho_{\text{FL}} = \Sigma_{\text{FL}}/h_{\text{FL}} = \mathcal{C}(T)\rho_{\text{ave}}$ can be derived from thermodynamic considerations associated with the coexistence between the bulk and the two-dimensional LJ phase comprising the first layer.

III. EXTENSION TO FINITE SYSTEMS

In this section we extend our investigation to finite systems. We are interested to see if the remarkable result of the previous section, namely, $\mathcal{C} = \mathcal{C}(T)$ independent of density, is also valid for these systems. Clearly, confinement effects will only begin to be important as the system scale becomes comparable to the characteristic scale of the layering phenomenon. Given the size of ℓ_c (~ 5), we would expect confinement to become important for $L \lesssim 20$ (for a slit geometry with two opposed boundaries).

Molecular-dynamics simulations in small nanoslits ($L = 15.9$) yield values of h_{FL} and Σ_{FL} that are up to 2% and 3% smaller than the infinite system values, respectively. For fluids under more considerable nanoconfinement ($L = 6.3$), MD simulations yield values of h_{FL} and Σ_{FL} up to 8% and 11% smaller than the infinite system values, respectively. In other words, although confinement has an effect on both h_{FL} and Σ_{FL}, the ratio of these two quantities remains relatively insensitive to ρ_{ave}. This trend is illustrated in Fig. 11. These results suggest that the relation $\mathcal{C} = \mathcal{C}(T)$, obtained

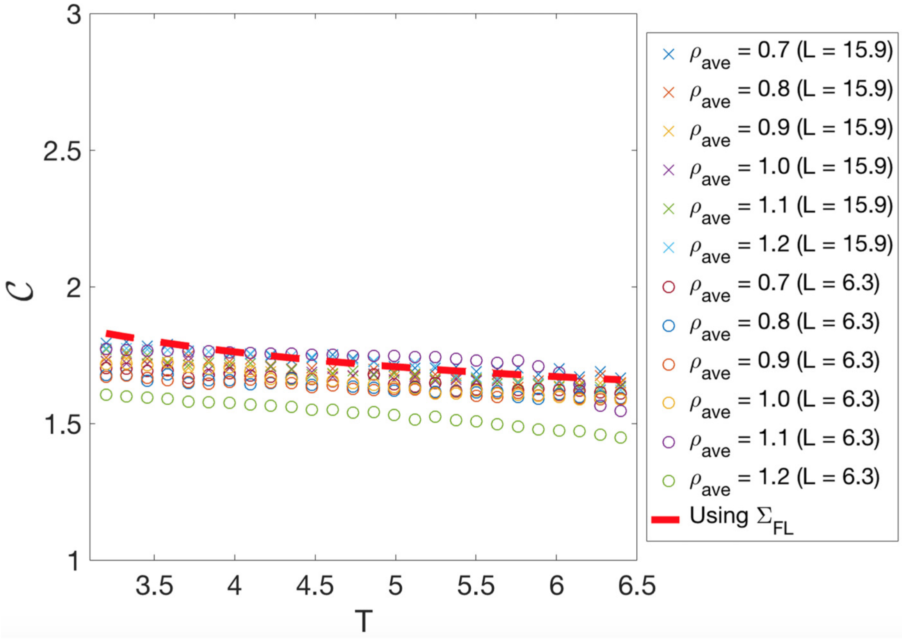

FIG. 11. Predicted value of $\mathcal{C}$, based on the value of Σ_{FL} from Eq. (18), shown against results from MD simulations of fluid confined within small systems ($L = 15.9$ and $L = 6.3$), with agreement within 12%.

for semi-infinite systems, remains approximately valid even under considerable confinement (at $L = 6.3$ the solid boundaries are so close that there is no region that clearly resembles bulk fluid, for any of the densities studied). Ultimately, we do expect a number of assumptions used in the present work to fail as L decreases further (most notably mean-field interaction); fortunately, however, it appears that this will lead to significant loss of accuracy only for very small systems ($L \lesssim 6$).

The key to the broad success of this scaling relation even at considerable nanoconfinement is the use of ρ_{ave} for characterizing the fluid density. As discussed in Ref. [19], although z_{min} is of atomistic size, its effect can be appreciable when the characteristic system length scale is also of the same order. By considering the actual volume available to the fluid (by excluding the standoff distance z_{min}), ρ_{ave} is a more appropriate measure of the fluid density than the density based on the distance between the solid boundaries (L) or the bulk density.

IV. SUMMARY AND DISCUSSION

Through a combination of molecular-mechanics arguments and MD simulations, we have elucidated several key relationships that characterize the appearance and structure of the fluid-solid interface for simple liquids. We have shown that layering is controlled by the balance between the wall-fluid interaction and the thermal energy, as quantified by the Wall number Wa. When $\text{Wa} \ll 1$, the fluid density profile near the solid exhibits little spatial inhomogeneity. It is worth noting that this conclusion is supported both by the MD simulations presented in Sec. II B and the Nernst-Planck theory presented in Sec. II C. In particular, for the former, we can see that in the limit of large T (i.e., $\text{Wa} \ll 1$, since n is fixed), $\mathcal{C}$ tends to unity, indicating the absence of layering. For the latter, we can see that Eq. (14) leads to $\rho_0 = \rho_{\text{ave}}$ in the limit $\text{Wa} \to 0$, also indicating a spatially uniform density profile.

Within the layering regime ($\text{Wa} \not\ll 1$), the density of the first layer can be represented as a multiplicative enhancement over the average fluid density. For dense fluids ($\rho \gtrsim 0.7$), this density enhancement is nearly independent of the average fluid density and only weakly dependent on temperature. We have also demonstrated that the areal densities of the first layer can be modeled to a good approximation level using a polynomial function of density and temperature. Moreover, we have shown that the width of the first layer is nearly linear in the system average density and exhibits little dependence on temperature. We have verified that our results generalize to fluids under considerable nanoconfinement as well as systems with a variety of wall boundary conditions and fluid-solid interaction strengths that permit the formation of layers.

Our results suggest that (over the broad range of densities and temperatures simulated) the primary lever for tuning Σ_{FL}, essentially the particle content of the first layer, is modification of ρ_{ave}. It is important to note that, as can be seen from the MD results in Fig. 5, the (nondimensional) temperature can also be used as a much weaker lever for tuning Σ_{FL} (and thus the fluid-solid interaction strength ε^* can also be used for the same purpose).

Additional MD simulations have shown our results to be insensitive to solid structure as well as solid-fluid interaction parameters, as long as $\text{Wa} \not\ll 1$ and the fluid is unable to infiltrate the solid. It is worth noting that a fluid bounded by graphene, owing to the high in-plane density of carbon atoms in graphene, will generally have a higher Wall number than that same fluid bounded by many other choices of solid. We also note that the results presented above are for simulations with rigid boundaries. Simulations with thermalized walls exhibit a small but measurable $[O(10\%)]$ reduction in the value of $\mathcal{C}$, attributed to boundary flexure into the fluid region.

In closing, we note that despite the focus on fluid-solid interfacial layers at equilibrium, we expect our results to be useful for nonequilibrium settings involving fluid flow and heat transport. We note that nonequilibrium MD simulations have shown that fluid flow in confined geometries does not appreciably affect fluid structure. Thus information about the equilibrium structure of the first layer should prove useful in the development of models that predict interfacial resistance to heat and momentum transport.

ACKNOWLEDGMENTS

This work was supported by the DOE CSGF under Contract No. DE-FG02-97ER25308. Computing resources were provided by the Center for Nanoscale Materials, a US Department of Energy, Office of Science, Office of Basic Energy Sciences User Facility, under Contract No. DE-AC02-06CH11357.

APPENDIX: MOLECULAR-DYNAMICS SIMULATIONS

In our simulations, graphene was modeled as a sheet of carbon atoms packed in a hexagonal lattice. To minimize edge effects, each graphene sheet measured at least 30×30 in the in-plane directions. For the semi-infinite systems described in Sec. II, the channel width was $L = 32$.

Interactions between carbon and fluid molecules were modeled using $\sigma^* = 3.15$ Å and $\varepsilon^* = 0.15\,\mathrm{kcal\,mol^{-1}}$, while interactions between fluid molecules were modeled using $\sigma_f^* = 3.15$ Å and $\varepsilon_f^* = 0.15\,\mathrm{kcal\,mol^{-1}}$. A cutoff distance of $4\sigma^*$ was used throughout.

Simulations were conducted in LAMMPS (large scale atomistic/molecular massively parallel simulator) [38] in the NVT ensemble using a Nosé-Hoover thermostat [39,40] within the range of densities $0.4 \leqslant \rho_{\mathrm{ave}} \leqslant 1.2$. The majority of simulations were conducted within $2 \leqslant T \leqslant 20$. The simulation time step was $1.25 \times 10^{-3}\tau$, where we define the LJ time unit as $\tau \equiv \sqrt{\frac{m\sigma^2}{\varepsilon}}$ and m is the mass of a fluid molecule. Each system was allowed to equilibrate for a time of 1875τ, after which samples were recorded every $1.25 \times 10^{-3}\tau$ for a total of 625τ. To facilitate convergence to the equilibrium density profile, each system was initialized with the equilibrium density profile at $T = 3.8$.

Below we discuss the robustness of our results by reporting their sensitivity to differing simulation parameters and conditions. In each case, the phrase "a subset of densities and temperatures" refers to $\rho_{\mathrm{ave}} \in \{0.4,0.8,1.2\}$ and $T \in \{3.2,6.4\}$.

1. Effect of boundary structure

All graphene sheets were of armchair chirality; for a subset of densities and temperatures we verified that chirality had no observable impact on any of the results reported here.

In order to quantify the effect of using a single-layer wall to model the solid boundaries, we performed simulations of semi-infinite systems with boundaries consisting of five layers of graphene for a subset of densities and temperatures. We found that none of the results reported above were observably affected by the presence of thicker bounding solids.

In particular, we note that we would not expect additional layers of graphene to have a significant effect on the standoff distance $z_{\min}$. A simple calculation shows that in the limiting case of a semi-infinite solid wall (infinite layers of solid), $z_{\min} = (\frac{2}{15})^{1/6}$, which differs from $z_{\min}$ for a single sheet by approximately 0.1. In practice, due to the cutoff, fluid near the wall could not respond to the presence of more than three layers of solid and so we expect the effect of multilayer boundaries on $z_{\min}$ to be even less than 0.1.

In order to quantify the effect of the graphene structure on our results, we also performed simulations of semi-infinite systems with solid boundaries resembling (100) silicon as well as silicon dioxide. In all cases, the range of temperatures simulated were such that $\mathrm{Wa} \lll 1$. We measured values for $\mathcal{C}$ that were negligibly different from those found for graphene.

2. Effect of boundary rigidity

For the results described above, all graphene sheets were kept rigid throughout each simulation. We investigated the effect of this assumption by simulating semi-infinite systems with boundaries consisting on multiple graphene sheets thermalized to the system temperature. Thermalization was performed via a Langevin thermostat [41]; the graphene layer furthest from the fluid was held rigid.

Interactions between atoms within the graphene were simulated using the optimized Tersoff potential [42]; interactions between atoms in different graphene sheets were simulated using the Girifalco potential for carbon structures [43]. Thermalized walls tend to intrude slightly into the fluid region, which in turn decreases the accessible channel width for fluid molecules.

For a subset of densities and temperatures, we observed within our MD simulations that flexure of the graphene boundary into the fluid region was bounded from above by a displacement of 2.6σ from the initial position $z^* = 0$ of the graphene sheet nearest the fluid; variations of the in-plane lattice structure were found to be negligible. The results exhibited very small differences in h_{FL} (less than 5%, as compared to the values reported in Sec. II, with no obvious trends) and small differences in Σ_{FL} and $\mathcal{C}$ (bounded from above by 8%, as compared to the values reported in Secs. II and II C 4). In particular, values of Σ_{FL} and $\mathcal{C}$ were found to be systematically lower, which suggests that boundary rigidity and in particular boundary flexure into the fluid region tend to have a measurable (but generally small) effect on the results presented in this paper. These results are similar to the findings in Sec. III; namely, the values of Σ_{FL} and $\mathcal{C}$ show weak but systematic deviations below the values corresponding to Eq. (18) in the limit of finite channel widths.

3. Effect of LJ parameters

To check robustness against changes in the LJ parameters, we performed semi-infinite simulations in which ε^* and ε_f^* were varied in the range $0.1\ \mathrm{kcal\ mol}^{-1} \leqslant \varepsilon^* = \varepsilon_f^* \leqslant 0.5\ \mathrm{kcal\ mol}^{-1}$ (while the two remained equal), as well as simulations in which the ratio of these two parameters varied in the range $0.5 \leqslant \varepsilon^*/\varepsilon_f^* \leqslant 1.2$. For a subset of densities and temperatures, these results differed by no more than ±7% (with no obvious trends) from the results reported in Secs. II and II C 4 for h_{FL}, Σ_{FL}, and $\mathcal{C}$.

---

[1] G. Hummer, J. C. Rasaiah, and J. P. Noworyta, Water conduction through the hydrophobic channel of a carbon nanotube, Nature (London) **414**, 188 (2001).

[2] M. Majumder, N. Chopra, R. Andrews, and B. J. Hinds, Nanoscale hydrodynamics: Enhanced flow in carbon nanotubes, Nature (London) **438**, 44 (2005).

[3] M. Whitby and N. Quirke, Fluid flow in carbon nanotubes and nanopipes, Nat. Nanotechnol. **2**, 87 (2007).

[4] J. K. Holt, H. G. Park, Y. Wang, M. Stadermann, A. B. Artyukhin, C. P. Grigoropoulos, A. Noy, and O. Bakajin, Fast mass transport through sub-2-nanometer carbon nanotubes, Science **312**, 1034 (2006).

[5] Y. You, V. Sahajwalla, M. Yoshimura, and R. K. Joshi, Graphene and graphene oxide for desalination, Nanoscale **8**, 117 (2016).

[6] T. Humplik, J. Lee, S. C. O'Hern, B. A. Fellman, M. A. Baig, S. F. Hassan, M. A. Atieh, F. Rahman, T. Laoui, R. Karnik, and E. N. Wang, Nanostructured materials for water desalination, Nanotechnology **22**, 292001 (2011).

[7] I. C. Bourg, L. E. Beckingham, and D. J. DePaolo, The nanoscale basis of CO_2 trapping for geologic storage, Environ. Sci. Technol. **49**, 10265 (2015).

[8] A. Siria, P. Poncharal, A.-L. Biance, R. Fulcrand, X. Blase, S. T. Purcell, and L. Bocquet, Giant osmotic energy conversion measured in a single transmembrane boron nitride nanotube, Nature (London) **494**, 455 (2013).

[9] B. J. Hinds, N. Chopra, T. Rantell, R. Andrews, V. Gavalas, and L. G. Bachas, Aligned multiwalled carbon nanotube membranes, Science **303**, 62 (2004).

[10] N. G. Portney and M. Ozkan, Nano-oncology: drug delivery, imaging, and sensing, Anal. Bioanal. Chem. **384**, 620 (2006).

[11] L. A. Rowley, D. Nicholson, and N. G. Parsonage, Grand ensemble Monte-Carlo studies of physical adsorption, Mol. Phys. **31**, 389 (1976).

[12] F. F. Abraham, The interfacial density profile of a Lennard-Jones fluid in contact with a (100) Lennard-Jones wall and its relationship to idealized fluid/wall systems: A Monte Carlo simulation, J. Chem. Phys. **68**, 3713 (1978).

[13] J. A. Thomas and A. J. H. McGaughey, Density, distribution, and orientation of water molecules inside and outside carbon nanotubes, J. Chem. Phys. **128**, 084715 (2008).

[14] P. A. Thompson and M. O. Robbins, Shear flow near solids: Epitaxial order and flow boundary conditions, Phys. Rev. A **41**, 6830 (1990).

[15] P. A. Thompson and M. O. Robbins, Origin of stick-slip motion in boundary lubrication, Science **250**, 792 (1990).

[16] Y. Liu, Q. Wang, T. Wu, and L. Zhang, Fluid structure and transport properties of water inside carbon nanotubes, J. Chem. Phys. **123**, 234701 (2005).

[17] J. Wang, Y. Zhu, J. Zhou, and X.-H. Lu, Diameter and helicity effects on static properties of water molecules confined in carbon nanotubes, Phys. Chem. Chem. Phys. **6**, 829 (2004).

[18] A. Alexiadis and S. Kassinos, The density of water in carbon nanotubes, Chem. Eng. Sci. **63**, 2047 (2008).

[19] G. J. Wang and N. G. Hadjiconstantinou, Why are fluid densities so low in carbon nanotubes? Phys. Fluids **27**, 052006 (2015).

[20] J. Israelachvili, *Intermolecular and Surface Forces* (Academic, New York, 1992).

[21] J. R. Henderson, Compressibility route to solvation structure, Mol. Phys. **59**, 89 (1986).

[22] J.-L. Barrat and L. Bocquet, Influence of wetting properties on hydrodynamic boundary conditions at a fluid/solid interface, Faraday Discuss. **112**, 119 (1999).

[23] D. A. Doshi, E. B. Watkins, J. N. Israelachvili, and J. Majewski, Reduced water density at hydrophobic surfaces: Effect of dissolved gases, Proc. Natl. Acad. Sci. USA **102**, 9458 (2005).

[24] S.-W. Hung, G. Kikugawa, and J. Shiomi, Mechanism of temperature dependent thermal transport across the interface between self-assembled monolayer and water, J. Phys. Chem. C **120**, 26678 (2016).

[25] Z. Tian, A. Marconnet, and G. Chen, Enhancing solid-liquid interface thermal transport using self-assembled monolayers, Appl. Phys. Lett. **106**, 211602 (2015).

[26] J. Muscatello, E. Chacón, P. Tarazona, and F. Bresme, Deconstructing Temperature Gradients Across Fluid Interfaces: The Structural Origin of the Thermal Resistance of Liquid-Vapor Interfaces, Phys. Rev. Lett. **119**, 045901 (2017).

[27] D. Alexeev, J. Chen, J. H. Walther, K. P. Giapis, P. Angelikopoulos, and P. Koumoutsakos, Kapitza resistance between few-layer graphene and water: Liquid layering effects, Nano Lett. **15**, 5744 (2015).

[28] M. C. Gordillo and J. Marti, Hydrogen bond structure of liquid water confined in nanotubes, Chem. Phys. Lett. **329**, 341 (2000).

[29] L.-L. Huang, Q. Shao, L.-H. Lu, X.-H. Lu, L.-Z. Zhang, J. Wang, and S.-Y. Jiang, Helicity and temperature effects on static properties of water molecules confined in modified carbon nanotubes, Phys. Chem. Chem. Phys. **8**, 3836 (2006).

[30] J. Chen, J. H. Walther, and P. Koumoutsakos, Strain engineering of Kapitza resistance in few-layer graphene, Nano Lett. **14**, 819 (2014).

[31] N. G. Hadjiconstantinou, Hybrid atomistic–continuum formulations and the moving contact-line problem, J. Comput. Phys. **154**, 245 (1999).

[32] J.-P. Hansen and I. R. McDonald, *Theory of Simple Liquids* (Elsevier, Amsterdam, 2006).

[33] I. Hanasaki and A. Nakatani, Flow structure of water in carbon nanotubes: Poiseuille type or plug-like? J. Chem. Phys. **124**, 144708 (2006).

[34] M. P. Allen and D. J. Tildesley, *Computer Simulation of Liquids* (Oxford University Press, Oxford, 1989).

[35] W. Humphrey, A. Dalke, and K. Schulten, VMD: Visual molecular dynamics, J. Mol. Graph. **14**, 33 (1996).

[36] A. V. Raghunathan, J. H. Park, and N. R. Aluru, Interatomic potential-based semiclassical theory for Lennard-Jones fluids, J. Chem. Phys. **127**, 174701 (2007).

[37] F. F. Abraham, The phases of two-dimensional matter, their transitions, and solid-state stability: A perspective via computer simulation of simple atomic systems, Phys. Rep. **80**, 340 (1981).

[38] S. Plimpton, Fast parallel algorithms for short-range molecular dynamics, J. Comput. Phys. **117**, 1 (1995).

[39] S. Nosé, A unified formulation of the constant temperature molecular dynamics methods, J. Chem. Phys. **81**, 511 (1984).

[40] W. G. Hoover, Canonical dynamics: Equilibrium phase-space distributions, Phys. Rev. A **31**, 1695 (1985).

[41] T. Schneider and E. Stoll, Molecular-dynamics study of a three-dimensional one-component model for distortive phase transitions, Phys. Rev. B **17**, 1302 (1978).

[42] J. Tersoff, Empirical Interatomic Potential for Carbon, with Applications to Amorphous Carbon, Phys. Rev. Lett. **61**, 2879 (1988).

[43] L. A. Girifalco, M. Hodak, and R. S. Lee, Carbon nanotubes, buckyballs, ropes, and a universal graphitic potential, Phys. Rev. B **62**, 13104 (2000).